Non-galvanic calibration and operation of a quantum dot thermometer

J. M. A. Chawner,* S. Holt, E. A. Laird, Yu. A. Pashkin, and J. R. Prance
Department of Physics, Lancaster University, Lancaster, LA1 4YB, United Kingdom

S. Barraud
CEA/LETI-MINATEC, CEA-Grenoble, 38000 Grenoble, France

M. F. Gonzalez-Zalba
Hitachi Cambridge Laboratory, J. J. Thomson Ave., Cambridge, CB3 0HE, United Kingdom†
(Dated: January 19, 2021)

A cryogenic quantum dot thermometer is calibrated and operated using only a single non-galvanic gate connection. The thermometer is probed with radio-frequency reflectometry and calibrated by fitting a physical model to the phase of the reflected radio-frequency signal taken at temperatures across a small range. Thermometry of the source and drain reservoirs of the dot is then performed by fitting the calibrated physical model to new phase data. The thermometer can operate at the transition between thermally broadened and lifetime broadened regimes, and outside the temperatures used in calibration. Electron thermometry was performed at temperatures between 3.0 K and 1.0 K, in both a 1 K cryostat and a dilution refrigerator. In principle, the experimental setup enables fast electron temperature readout with a sensitivity of $4.0 \pm 0.3\,\mathrm{mK}/\sqrt{\mathrm{Hz}}$, at kelvin temperatures. The non-galvanic calibration process gives a readout of physical parameters, such as the quantum dot lever arm. The demodulator used for reflectometry readout is readily available and very affordable.

I. INTRODUCTION

Electron temperature is a fundamental parameter that can limit the performance of low-temperature experiments and applications. Electron thermometry is an essential tool in understating the behaviour of low-temperature circuitry [1], for example the processors used in quantum computers or devices used to study exotic electronic phases and materials. Accurate and fast electron temperature readout is also a valuable tool for thermodynamic experiments. Increasingly sensitive quantum circuits require delicate and non-invasive electronic thermometry. Quantum dot (QD) and single-electron transistor (SET) conduction thermometry are well established as a powerful approach to monitor electron temperatures [1–11]. However, these thermometers require the measurement of current through the QD, which can complicate or interfere with other electronic measurements in the experiment. Furthermore, the extra galvanic connections for dot thermometry can be a source of additional noise and parasitic heating. Local charge sensing can be used to probe the occupation of a QD without having to pass a direct current through it [5, 12–15]. This approach still requires galvanic connections to read the charge sensor. Similarly, radio frequency (RF) reflectometry techniques have recently allowed QD thermometry to be performed without measuring current through the QD, which is effective outside the lifetime broadened regime [16, 17]. However, for both charge sensing and reflectometry, connections to the source and drain of the dot are still needed to measure the dot lever arm for calibration.

Here we demonstrate how a completely non-galvanic QD thermometer can be calibrated and used with a single capacitive gate connection, including a calibration of the lever arm with no DC source-drain bias. The QD thermometer has the flexibility to be used on any conducting reservoir and operates in an intermediate regime where the maximum temperature is much lower than the QD charging energy $k_\mathrm{B}T \ll E_\mathrm{c}$ and the minimum temperature is similar to the tunnel coupling $k_\mathrm{B}T \sim \hbar\Gamma$.

II. EXPERIMENTAL DETAILS

The QD device used in our experiment is a silicon-on-insulator trigate accumulation-mode field-effect transistor (FET) with a channel length, width and height of 80 nm, 30 nm and 10 nm respectively, shown in Fig 1a and b. For more details about the device, see reference [18]. At cryogenic temperatures, when a positive sub-threshold DC voltage V_tg is applied to the top gate, a localisation potential appears in the Si channel underneath the gate. This allows bound electron states to accumulate, and creates a single QD. Corner dots [19, 20] do not appear in the structure due to the narrow width of the channel. The FET top gate also acts as a plunger gate for the QD via capacitance C_tg, allowing tuning of the next available energy level in the QD, which is labelled E_QD, by adjusting V_tg. The source and drain electrodes are both grounded and act as a single reservoir of electrons with a Fermi level μ (Fig 1c). Throughout the experiment, the back gate was grounded.

The QD energy level E_QD is broadened by tunnel coupling to the reservoir [21, 22]. This is described with a broadened density of states in the form of a normalised Lorentzian, given by:

$$n(E_\mathrm{QD}, E) = \frac{1}{\pi}\frac{\hbar\Gamma}{(E_\mathrm{QD}-E)^2 + (\hbar\Gamma)^2}, \qquad (1)$$

where $\hbar$ is the reduced Planck's constant [21]. The tun-

* j.chawner@lancaster.ac.uk
† Present address: Quantum Motion Technologies, Windsor House, Cornwall Road, Harrogate, England, HG1 2PW

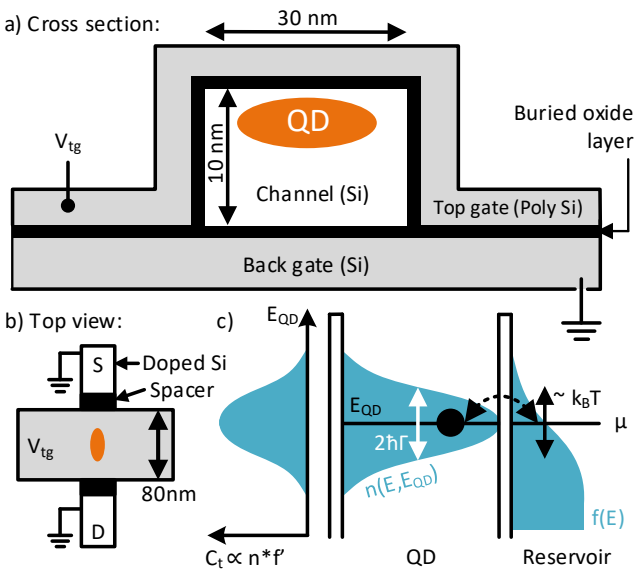

FIG. 1. Details of the silicon field-effect transistor QD. **a)** Cross-section schematic of the device. The transistor consists of an undoped 1-D Si channel, 10 nm high by 30 nm wide, with n-doped Si source-drain connections. A polycrystalline silicon top gate, 80 nm wide, bridges over the channel, separated by a layer of SiO_2. A grounded Si back gate is beneath the channel, separated from the channel by 145 nm thick buried SiO_2. **b)** Top view of device. The source (S) and drain (D) channel connection points are n-doped and behave as a single grounded reservoir during thermometry operation. Two spacers are used to prevent doping of the Si channel under the top gate. **c)** Energy diagram of the system. The reservoir has an occupation of electron states given by the Fermi-Dirac distribution f. The QD energy level E_{QD} is broadened from tunnel coupling to the reservoir, with a density of states n described by Eq. (1). The tunnelling capacitance C_t as a function of E_{QD} has a shape proportional to $f' * n$.

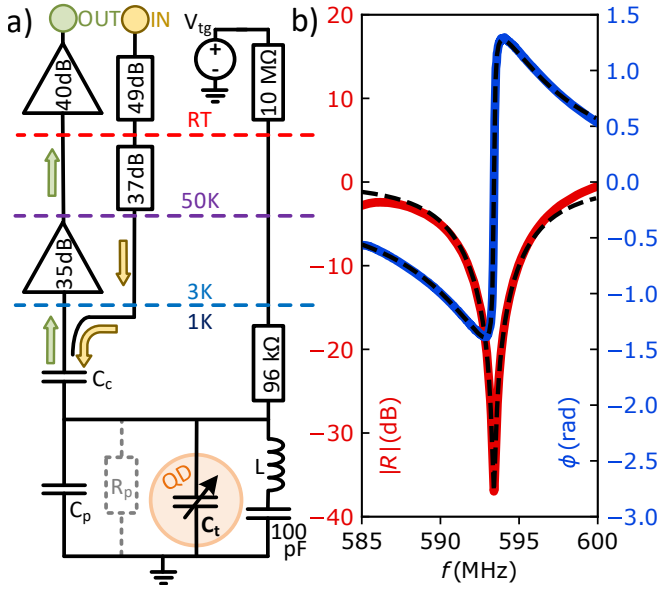

FIG. 2. Details of RF circuitry. **a)** Schematic of the circuit layout. The resonant circuit is comprised of the NbTiN-on-quartz spiral inductor L, the parasitic capacitance C_p, coupling capacitance C_c and the variable QD tunnelling capacitance C_t, which is the physical parameter monitored for thermometry. C_p includes the geometric gate capacitance C_{tg} for modelling purposes. R_p is a modelled parasitic loss resistance to ground which impacts the resonant circuit Q-factor. The inductor line has a 100 pF capacitor to provide a DC break between the top gate and ground. The 96 kΩ resistor limits top gate RF signal loss to the DC line. V_{tg} is the controllable DC top gate voltage. IN and OUT represent the RF reflectometry input and output signal, respectively. **b)** The loaded measurement circuit resonance when coupled to the top gate, with the reflected signal magnitude $|R|$ and phase ϕ shown in red and blue, respectively. The black dashed lines show the fitted circuit model, which measures a Q-factor of 63. Thermometry is performed on resonance at $f_0 = 593$ MHz, where phase is most responsive.

nel rate Γ between the QD and the reservoir is given by $\Gamma = \Gamma_s\Gamma_d/(\Gamma_s + \Gamma_d)$, where Γ_s(d) is the tunnel rate through source(drain) barrier. The probability P_{QD} of an excess electron occupying the QD is given by the integral of the product of $n(E_{QD}, E)$ and the Fermi-Dirac distribution of electrons in the reservoir $f(E)$ [21]:

$$P_{QD}(E_{QD}) = \int_{-\infty}^{\infty} f(E)n(E_{QD}, E)\mathrm{d}E. \tag{2}$$

This is the convolution of the two functions, so P_{QD} becomes:

$$P_{QD}(E_{QD}) = (f * n). \tag{3}$$

Due to the spin degeneracy of the extra electron in the QD, $P_{QD} = 1/2$ occurs when $E_{QD} = \mu \pm k_B T \ln 2$ [17, 23]. The QD has both a constant geometric capacitance and a variable 'tunneling' capacitance C_t, given by [17, 24–28]:

$$C_t(V_{tg}) = e\alpha\frac{\partial P_{QD}}{\partial V_{tg}}, \tag{4}$$

where $\alpha = C_{tg}/C_\Sigma$ is the top gate lever arm, C_Σ is the total QD capacitance, $\partial V_{tg} = -\partial E_{QD}/e\alpha$, and e is the elementary charge. Inserting Eq. (3) into this definition gives us the tunnelling capacitance of the QD-reservoir system:

$$C_t(V_{tg}) = e\alpha(f * n)' = e\alpha(f' * n). \tag{5}$$

The derivative of f with respect to V_{tg}, denoted f', is

$$f'(V_{tg}) = \frac{1}{4k_B T_e}\cosh^{-2}\left(\frac{-\alpha e(V_{tg} - V_0)}{2k_B T_e}\right), \tag{6}$$

where T_e is the electron temperature of the reservoirs, V_0 is the value of V_{tg} when $P_{QD} = 1/2$, and k_B is the Boltzmann constant. The T_e dependence of C_t via Eq. (6) is the basis for the non-galvanic QD thermometer.

The capacitance C_t was measured by RF reflectometry using the setup shown in Fig 2a. A resonant circuit was connected to the QD top gate and consisted of a NbTiN-on-quartz spiral inductor $L = 96$ nH, and a coupling capacitor $C_c = 0.18$ pF. The inductor is placed parallel to the measured capacitance to help improve the loaded Q-factor, which helps achieve higher responsiveness to a change in capacitance [29]. Modelling the circuit using the measured RF reflection $|R|$ and

phase ϕ (shown in Fig 2b) gives a resonance frequency of $f_0 = 593.4\,\text{MHz}$ with a Q-factor of 63, a parasitic capacitance of $C_\text{p} = 0.57\,\text{pF}$ and a parasitic resistance of $R_\text{p} = 43.2\,\text{k}\Omega$. A modelled circuit loss to ground is represented by resistance R_p, which affects the resonance Q-factor [29]. The parasitic capacitance C_p includes the geometric gate capacitance C_tg. The demodulation of $|R|$ and ϕ was performed with an 'ADL5387' active quadrature demodulator chip. To allow a DC bias V_tg to be applied to the top gate, a 100 pF capacitor was placed after the inductor to avoid DC-shorting the device and to create a good RF ground at the frequency of operation. A 96 kΩ resistor was used to prevent RF signals from escaping via the DC bias line. The resonant frequency depends on total top gate capacitance via $f_0 = 1/2\pi\sqrt{L(C_\text{c}+C_\text{p}+C_\text{t})}$. At the circuit resonant frequency, $\phi \propto C_\text{t}$, when $C_\text{t} \ll C_\text{p} + C_\text{c}$ [17, 28, 30–32]. This gives a change in reflected signal phase that depends on T_e according to:

$$\phi - \phi_0 = Ae\alpha\left(f' * n\right), \tag{7}$$

where A is a fitting constant, which tells us the phase change due to a small change in capacitance, and ϕ_0 is the circuit phase offset at the resonant frequency when $C_\text{t} \approx 0$. If the constants A, α and Γ are known, measuring $\phi - \phi_0$ as a function of $V_\text{tg} - V_0$ and fitting the model described by Eq. (7) gives a readout of electron temperature T_e. A demonstration of this technique is shown in Fig 3.

III. RESULTS

The QD thermometer was measured in two fridge systems: a cryogen-free 1 K cryostat[1] and a cryogen-free dilution refrigerator[2], where it was calibrated and operated. In both systems, the fridge temperature was monitored by a ruthenium oxide resistance fridge thermometer[3] mounted alongside the QD thermometer during data collection. The reading of the ruthenium oxide fridge thermometer is denoted as T_f.

In the 1 K cryostat, calibration was done by reading the reflected signal phase across a number of sweeps of V_tg at a set of fridge temperatures $T_\text{f} = 2.0, 2.5, 3.0\,\text{K}$. A single least-squares fit using Eq. (7) was performed on the collective phase traces for this set of temperatures (Fig 3). It was assumed that the electron temperature is well thermalised with the fridge temperature at 2 K and above, and so during the calibration the condition $T_\text{e} = T_\text{f}$ was applied to Eq. (7). For each phase trace, ϕ_0 and V_0 were individually fitted. The calibration fit produced an estimate for the values $\alpha = 0.74 \pm 0.02$, $\Gamma = 270 \pm 20\,\text{ns}^{-1}$ and $A = 5.13 \pm 0.06\,\text{rad}\,\text{pF}^{-1}$. This implies $\Gamma \gg 2\pi f_0$, therefore dissipative components were neglected and the cyclic tunnelling was considered adiabatic. With these three constants defined, the thermometer was calibrated and ready for operation.

[1] Oxford Instruments 'Io'
[2] BlueFors 'LD250'
[3] Model ref 'ROTH-GEN' in the 1K cryostat and 'RuO2.RX-102B' in the dilution refrigerator

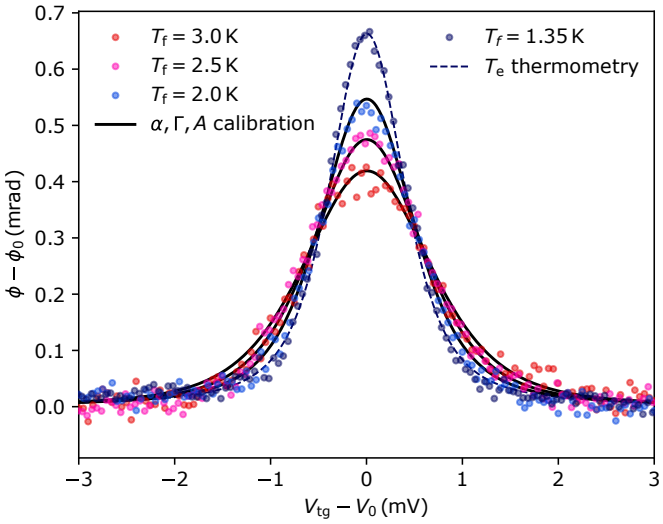

FIG. 3. QD thermometer calibration in 1 K cryostat, showing three experimental phase traces taken at fridge temperatures $T_\text{f} = 2.0, 2.5, 3.0\,\text{K}$. Each trace shows the change in reflected signal phase $\phi - \phi_0$ against top gate voltage $V_\text{tg} - V_0$ around the Coulomb peak of the QD. The solid black lines show the least-square fit of Eq. (7) onto the data, assuming the electron temperature T_e equals the fridge thermometer readout T_f. This calibration procedure estimates $\alpha = 0.74 \pm 0.02$, $\Gamma = 270 \pm 20\,\text{ns}^{-1}$ and $A = 5.13 \pm 0.06\,\text{rad}\,\text{pF}^{-1}$. These three constants are then included within Eq. (7), allowing electron thermometry to be performed, shown here with a T_e fit to data taken at $T_\text{f} = 1.35\,\text{K}$, yielding an electron temperature $T_\text{e} = 1.4 \pm 0.1\,\text{K}$

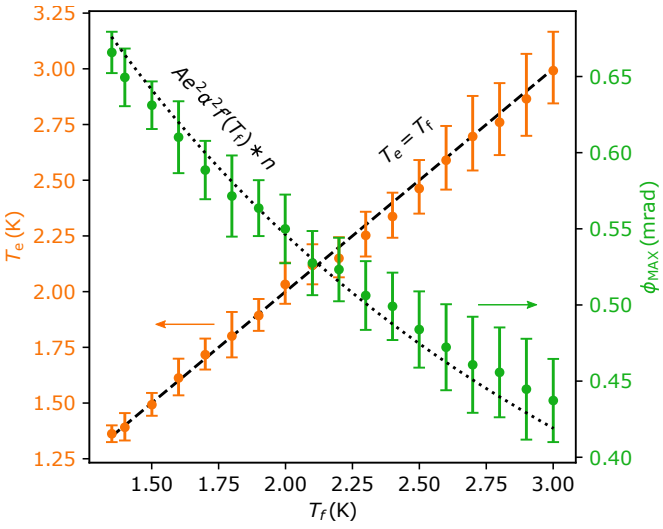

FIG. 4. Electron temperature T_e (orange) and max phase ϕ_MAX (green) readout from QD thermometer in 1 K cryostat. Thermometry readout was generated by fitting T_e, via calibrated Eq. (7), to the phase curve observed by sweeping the V_tg over the QD Coulomb peak. The peak phase ϕ_MAX was measured at $V_\text{tg} = V_0$, with no fitting process required. The fridge temperature T_f was read from a ruthenium oxide fridge thermometer thermally linked to the QD device. The dashed line highlights where $T_\text{e} = T_\text{f}$. The dotted line represents the model prediction from calibrated Eq. (7), assuming $T_\text{e} = T_\text{f}$.

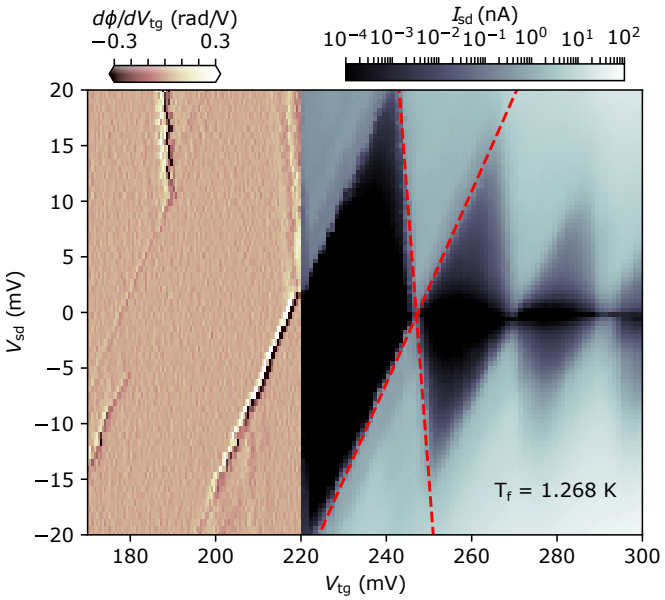

FIG. 5. Charge stability diagram measured by reflectometry technique and DC transport in 1 K cryostat. To the left of $V_{tg} = 220\,\text{mV}$, the derivative of reflected signal phase with respect to the top gate voltage $\mathrm{d}\phi/\mathrm{d}V_{tg}$ is plotted, demonstrating the non-galvanic reflectometry technique. For this measurement, the source and drain connections were grounded. To the right of $V_{tg} = 220\,\text{mV}$, the QD source-drain current $|I_{sd}|$ is plotted in log scale. The fridge temperature was $T_f = 1.268 \pm 0.001\,\text{K}$. Red lines highlight the source-drain gradients that match the calibration fit lever arm prediction, $\alpha = 0.74 \pm 0.02$, via Eq. (8), crossing at the QD Coulomb peak where the thermometry took place. Here the on-resonance current has a order of magnitude $I_{sd} \approx 1 - 10\,\text{nA}$, which is similar to the single-electron current defined by the calibration fit tunnel rate $e\Gamma \sim 6.9 \pm 0.5\,\text{nA}$.

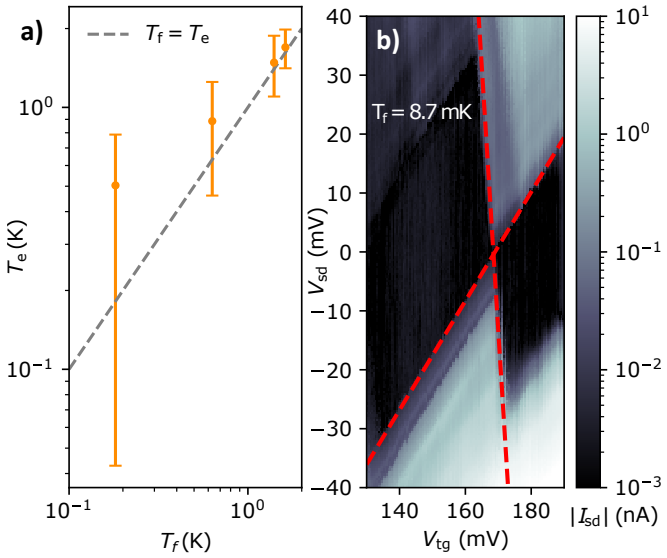

FIG. 6. QD Thermometry and stability diagram from dilution refrigerator measurements. **a)** Re-calibrated QD thermometer readout of electron temperature T_e compared with fridge thermometer readout T_f, measured near the device within the dilution refrigerator. The QD and fridge thermometers start to disagree below 1 K, but still agree within one standard deviation of confidence (For details on how the error is determined, see section II in the Supplemental Material [33]). **b)** Source-drain current stability diagram of QD mounted in dilution refrigerator. The temperature of the fridge was held at $T_f = 8.70 \pm 0.05\,\text{mK}$. Red lines highlight the source-drain gradients that match the calibration fit lever arm prediction, $\alpha = 0.84 \pm 0.03$, via Eq. (8), crossing at the QD Coulomb peak where the thermometry took place.

To use the QD thermometer, $\phi - \phi_0$ was measured as a function of $V_{tg} - V_0$ and fitted with the calibrated Eq. (7) to give a readout of electron temperature T_e. A series of thermometry readings were taken at varying fridge temperatures between 3.0 K and 1.3 K. Fridge temperature T_f was monitored for each QD thermometer reading of T_e (Fig 4). The QD thermometer agreed with the fridge thermometer across the range of temperatures, even at temperatures below the calibration range. It is worth noting that this works in the intermediate regime where $k_B T \sim \hbar\Gamma$ because the tunnel broadening is taken into account within the physical model. For quicker electron temperature readout, the QD can be tuned to where $V_{tg} = V_0$ so that $\phi - \phi_0 = \phi_{MAX}$, which was directly converted to a electron temperature via Eq. (7), using the previously calibrated values of α, Γ and A. This approach worked effectively, even at fridge temperatures below the calibration data.

Finally, to provide an independent confirmation of the calibration process, the QD source and drain connections were ungrounded to apply a source-drain voltage V_{sd} across the QD and measure a charge stability diagram of the device. Using the relationship

$$\alpha = \frac{1}{m_d - m_s}, \tag{8}$$

where $m_d = \Delta V_{tg}^d / \Delta V_{sd}^d$ is the gradient along the the 'drain resonance' side of a Coulomb diamond and $m_s = \Delta V_{tg}^s / \Delta V_{sd}^s$ is the 'source resonance' side, we can see the lever arm $\alpha = 0.74 \pm 0.02$ matches well with the Coulomb diamond geometry in Fig 5. This demonstrates that the lever arm of a QD can be obtained using one non-galvanic gate connection and measurements spanning a range of fridge temperatures. The order of magnitude of source-drain current $|I_{sd}|$ from the unblockaded QD was found to be in the order of $\sim 10\,\text{nA}$. This agrees with the calibration fit of the total tunnel rate constant $270 \pm 20\,\text{ns}^{-1}$, which equates to a source-drain current of $e\Gamma = 6.9 \pm 0.5\,\text{nA}$ for a single electron transport channel.

To study operation at lower temperatures, the QD thermometer was mounted into a dilution refrigerator. The calibration fit was performed as described above, with phase data taken at 1300 mK and 1600 mK. Within this system, the three calibration constants were found to be $\alpha = 0.84 \pm 0.03$, $\Gamma = 510 \pm 10\,\text{ns}^{-1}$ and $A = 0.75 \pm 0.07\,\text{rad}\,\text{pF}^{-1}$. The change in A is attributed to the differences between the two fridge systems affecting the RF electronics, such as parasitic capacitance C_p changing due to a different metallic geometry near to the QD chip. Both α and Γ are sensitive to the shape and position of the QD in the Si channel, which are likely to be different after a thermal cycle of the device.

The electron temperature readout T_e from the QD ther-

mometer in the dilution refrigerator agreed with the fridge temperature readout T_f above 1 K, despite the fact that $k_B T_f < \hbar\Gamma$ (Fig 6a). Below 1 K there was deviation of T_e away from T_f, although the point $T_e = T_f$ remains within one standard deviation of experimental uncertainty (For details on how the error is determined, see section II in the Supplemental Material [33]). The deviation of T_e readout and its increase in uncertainty occurs because the QD energy level is strongly tunnel-broadened and the response of the phase trace to temperature becomes weaker (For details on the influence of tunnel broadening, see section III and FIG. 4 in the Supplemental Material [33]). With a reduced Γ the QD thermometer would work at lower temperatures. This can be achieved by adjusting the device design geometry. Checking the charge stability diagram, the predicted lever arm $\alpha = 0.84 \pm 0.03$ matches the Coulomb diamond geometry well (Fig 6b). The dilution refrigerator experiment has an effective white noise phase sensitivity of $1.1 \pm 0.1\,\mu\text{rad}/\sqrt{\text{Hz}}$, in this case dominated by the measurement chain. With this equipment and the ϕ_{MAX} measurements demonstrated in Fig 4, the QD thermometer setup could achieve a potential sensitivity of $11 \pm 1\,\text{mK}/\sqrt{\text{Hz}}$ at 3.0 K, and $4.0 \pm 0.3\,\text{mK}/\sqrt{\text{Hz}}$ at 1.3 K (For details on the thermometer sensitivity, see section I in the Supplemental Material [33]).

IV. CONCLUSIONS

We have described the successful calibration and operation of a QD thermometer readout via a single capacitive connection in two separate cryostats, which introduces a new level of simplicity and versatility for measuring electron temperature. The calibration uses limited data to generate a physical model of the QD-reservoir system, which correctly estimates physical parameters such as the QD lever arm. Electron thermometry was successfully performed with the calibrated QD thermometer in a 1.0 K to 3.0 K range. The QD thermometer was also used for faster readout by monitoring the phase when the QD has an occupation probability of $1/2$. In this mode of operation, the noise floor of the measurement should allow for a sensitivity of $4.0 \pm 0.3\,\text{mK}/\sqrt{\text{Hz}}$ and $11 \pm 1\,\text{mK}/\sqrt{\text{Hz}}$, at 1.3 K and 3.0 K respectively. This process worked with the same QD chip in both cryostats. The QD thermometer can operate even in the case where $k_B T_e < \hbar\Gamma$, however with the system and techniques used here, the thermometry uncertainty starts to increase below 1 K due to strong tunnel coupling overriding the temperature dependence. Careful analysis of the thermometry uncertainty reveals the coldest limit of the QD thermometer, when the electron temperature readout confidence boundary increases beyond a usable size. A redesign of the QD device to reduce the tunnel rate would be needed to decrease the uncertainty at lower temperatures. The ability to fully calibrate and operate a non-galvanic electron thermometer with a single RF line simplifies the application of the device substantially. This device provides a versatile, sensitive and effective tool for monitoring electron temperature in nanoelectronic devices at cryogenic temperatures.

ACKNOWLEDGMENTS

We thank Xiao Collins, Kunal Lulla Ramrakhiyani, Michael Thompson and Alex Jones for their assistance.

This work was funded and supported by the European Microkelvin Platform (the European Union's Horizon 2020 research and innovation programme, Grant Agreement No. 824109), the UK EPSRC (EP/N019199/1), the ERC (818751) and Hitachi Europe Ltd.

The data that support the findings of this study are available at https://doi.org/10.17635/lancaster/researchdata/403, including descriptions of the data sets.

[1] F. Giazotto, T. T. Heikkilä, A. Luukanen, A. M. Savin, and J. P. Pekola, Rev. Mod. Phys. **78**, 217 (2006).
[2] C. Beenakker, Phys. Rev. B **44**, 1646 (1991).
[3] J. Pekola, K. Hirvi, J. Kauppinen, and M. Paalanen, Phys. Rev. Lett. **73**, 2903 (1994).
[4] L. Spietz, K. Lehnert, I. Siddiqi, and R. Schoelkopf, Science **300**, 1929 (2003).
[5] D. Maradan, L. Casparis, T.-M. Liu, D. Biesinger, C. Scheller, D. Zumbühl, J. Zimmerman, and A. Gossard, J. Low Temp. Phys. **175**, 784 (2014).
[6] J. V. Koski, A. Kutvonen, I. M. Khaymovich, T. Ala-Nissila, and J. P. Pekola, Phys. Rev. Lett. **115**, 260602 (2015).
[7] D. I. Bradley, R. E. George, D. Gunnarsson, R. P. Haley, H. Heikkinen, Y. A. Pashkin, J. Penttilä, J. R. Prance, M. Prunnila, L. Roschier, *et al.*, Nat. Commun. **7**, 1 (2016).
[8] O. Hahtela, E. Mykkänen, A. Kemppinen, M. Meschke, M. Prunnila, D. Gunnarsson, L. Roschier, J. Penttilä, and J. Pekola, Metrologia **54**, 69 (2016).
[9] Z. Iftikhar, A. Anthore, S. Jezouin, F. Parmentier, Y. Jin, A. Cavanna, A. Ouerghi, U. Gennser, and F. Pierre, Nat. Commun. **7**, 1 (2016).
[10] G. Nicolí, P. Märki, B. A. Bräm, M. P. Röösli, S. Hennel, A. Hofmann, C. Reichl, W. Wegscheider, T. Ihn, and K. Ensslin, Rev. Sci. Instrum. **90**, 113901 (2019).
[11] A. Jones, C. Scheller, J. Prance, Y. Kalyoncu, D. Zumbühl, and R. Haley, J. Low Temp. Phys. (2020).
[12] L. DiCarlo, H. Lynch, A. Johnson, L. Childress, K. Crockett, C. Marcus, M. Hanson, and A. Gossard, Phys. Rev. Lett. **92**, 226801 (2004).
[13] P. Torresani, M. Martínez-Pérez, S. Gasparinetti, J. Renard, G. Biasiol, L. Sorba, F. Giazotto, and S. De Franceschi, Phys. Rev. B **88**, 245304 (2013).
[14] A. Mavalankar, S. Chorley, J. Griffiths, G. Jones, I. Farrer, D. Ritchie, and C. Smith, Appl. Phys. Lett. **103**, 133116 (2013).
[15] J. Prance, C. Smith, J. Griffiths, S. Chorley, D. Anderson, G. Jones, I. Farrer, and D. Ritchie, Phys. Rev. Lett. **102**, 146602 (2009).
[16] S. Gasparinetti, K. Viisanen, O.-P. Saira, T. Faivre, M. Arzeo, M. Meschke, and J. Pekola, Phys. Rev. Appl. **3**, 014007 (2015).
[17] I. Ahmed, A. Chatterjee, S. Barraud, J. J. Morton, J. A. Haigh, and M. F. Gonzalez-Zalba, Commun. Phys. **1**, 1 (2018).

[18] A. Betz, S. Barraud, Q. Wilmart, B. Placais, X. Jehl, M. Sanquer, and M. Gonzalez-Zalba, Appl. Phys. Lett. **104**, 043106 (2014).

[19] B. Voisin, V.-H. Nguyen, J. Renard, X. Jehl, S. Barraud, F. Triozon, M. Vinet, I. Duchemin, Y.-M. Niquet, S. De Franceschi, *et al.*, Nano letters **14**, 2094 (2014).

[20] D. J. Ibberson, L. Bourdet, J. C. Abadillo-Uriel, I. Ahmed, S. Barraud, M. J. Calderón, Y.-M. Niquet, and M. F. Gonzalez-Zalba, Appl. Phys. Lett. **113**, 053104 (2018).

[21] L. P. Kouwenhoven, C. M. Marcus, P. L. McEuen, S. Tarucha, R. M. Westervelt, and N. S. Wingreen, in *Mesoscopic electron transport* (Springer, 1997) pp. 105–214.

[22] T. Ihn, *Semiconductor Nanostructures: Quantum States and Electronic Transport* (OUP Oxford, 2010).

[23] N. Hartman, C. Olsen, S. Lüscher, M. Samani, S. Fallahi, G. C. Gardner, M. Manfra, and J. Folk, Nat. Phys. **14**, 1083 (2018).

[24] M. Esterli, R. Otxoa, and M. Gonzalez-Zalba, Appl. Phys. Lett. **114**, 253505 (2019).

[25] R. Mizuta, R. Otxoa, A. Betz, and M. F. Gonzalez-Zalba, Phys. Rev. B **95**, 045414 (2017).

[26] S. Shevchenko, A. Omelyanchouk, and E. Il'ichev, J. Low Temp. Phys. **38**, 283 (2012).

[27] S. Shevchenko, S. Ashhab, and F. Nori, Phys. Rev. B **85**, 094502 (2012).

[28] G. Johansson, L. Tornberg, V. Shumeiko, and G. Wendin, J. Phys. Condens. Matter **18**, S901 (2006).

[29] I. Ahmed, J. A. Haigh, S. Schaal, S. Barraud, Y. Zhu, C.-m. Lee, M. Amado, J. W. Robinson, A. Rossi, J. J. Morton, *et al.*, Phys. Rev. Appl. **10**, 014018 (2018).

[30] S. Chorley, J. Wabnig, Z. Penfold-Fitch, K. Petersson, J. Frake, C. Smith, and M. Buitelaar, Phys. Rev. Lett. **108**, 036802 (2012).

[31] A. Betz, R. Wacquez, M. Vinet, X. Jehl, A. Saraiva, M. Sanquer, A. Ferguson, and M. Gonzalez-Zalba, Nano Lett. **15**, 4622 (2015).

[32] M. F. Gonzalez-Zalba, S. N. Shevchenko, S. Barraud, J. R. Johansson, A. J. Ferguson, F. Nori, and A. C. Betz, Nano Lett. **16**, 1614 (2016).

[33] *See Supplemental Material at [URL will be inserted by publisher] for extra material on the quantum dot thermometer temperature sensitivity, electron thermometry error, qunatum dot energy scales and coulomb peak location temperature dependence.*

[34] W. H. Press, S. A. Teukolsky, W. T. Vetterling, and B. P. Flannery, *Numerical recipes 3rd edition: The art of scientific computing* (Cambridge university press, 2007).